High-Speed Electrochemical Imaging

Dmitry Momotenko, Joshua C. Byers, Kim McKelvey,[†] Minkyung Kang, and Patrick R. Unwin[*]

Department of Chemistry, University of Warwick, Coventry CV4 7AL, United Kingdom. [†]Present address: Department of Electrical Engineering, University of Notre Dame, Notre Dame, IN 46556, USA.

ABSTRACT The design, development, and application of high-speed scanning electrochemical probe microscopy is reported. The approach allows the acquisition of a series of high-resolution images (typically 1000 pixels μm^{-2}) at rates approaching 4 seconds per frame, while collecting up to 8000 image pixels per second, about 1000 times faster than typical imaging speeds used up to now. The focus is on scanning electrochemical cell microscopy (SECCM), but the principles and practicalities are applicable to many electrochemical imaging methods. The versatility of the high-speed scan concept is demonstrated at a variety of substrates, including imaging the electroactivity of a patterned self-assembled monolayer on gold, visualization of chemical reactions occurring at single wall carbon nanotubes, and probing nanoscale electrocatalysts for water splitting. These studies provide movies of spatial variations of electrochemical fluxes as a function of potential and a platform for the further development of high speed scanning with other electrochemical imaging techniques.

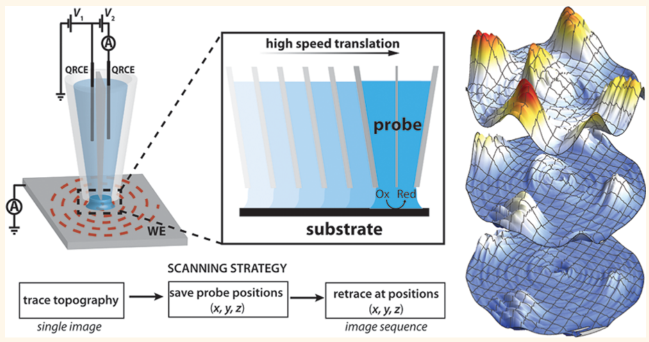

KEYWORDS: high-speed scanning · electrochemical imaging · scanning electrochemical cell microscopy · self-assembled monolayer · carbon nanotube · nanoparticle · electrocatalysis

Scanning probe microscopy (SPM) techniques offer tremendous capabilities for the structural and functional characterization of interfaces, which cannot be accessed by custom microscopic tools. However, while providing very high resolving power (down to the single atom level),[1] the time resolution (image acquisition rate) of SPMs has traditionally been constrained by factors such as the resonant frequencies of the piezoelectric actuators of the positioning system[2] as well as the intrinsic response time of the scanning probe itself. An important aspect of SPM development is thus to improve scanning rates, which now approach 1300 frames per second (fps) with advances in high-speed scanning tunneling (STM) and atomic force microscopy (AFM) techniques.[3−7]

In contrast, electrochemical probe imaging techniques cannot presently reach anywhere near such high scan dynamics for reasons that are discussed below. This is an issue because such techniques bring distinct attributes for noncontact visualization of interfacial processes (chemical concentrations, speciation and flux imaging), and improvements in image acquisition time would thus be hugely beneficial for probing and understanding surface chemistry. Although very well established techniques, like scanning electrochemical microscopy (SECM),[8−10] have been implemented in a variety of research applications, from the scanning of electrocatalyst libraries[11,12] to the read-out of enzymatic activity for bioassays,[13] and the *in situ* examination of living cell metabolism,[14,15] the slow probe scan rates present a severe limitation for the number of images that can be recorded, impacting greatly on the level of dynamic information that can be obtained.

In a typical scanning electrochemical probe microscopy (SEPM) setup, effective probe translation rates typically do not exceed one (or a few) tip radius per second due to (i) the relatively slow time constant of amperometric microelectrode probes (time required to establish the diffusion layer near the electrode),[16] which has usually required imaging in a repetitive move-stop-measure routine, slowing down the imaging process; and (ii) the rate of data acquisition, limited by the electronics capabilities (potentiostats, current−voltage converters, *etc.*). The rate of the probe positional feedback response, if employed, also has to be considered.[17−22] As a consequence, the duration of SEPM

* Address correspondence to p.r.unwin@warwick.ac.uk.

Received for review May 8, 2015 and accepted August 12, 2015.

Published online August 12, 2015
10.1021/acsnano.5b02792

experiments typically ranges from several tens of minutes to a few hours per image frame. Within such a time scale sample aging, probe and/or sample fouling, drift or change of experimental conditions (*e.g.*, temperature, solution composition *etc.*) may become a serious issue and usually only a single image or a few snapshots at a given set of experimental parameters can be recorded, often over a rather limited area. Attempting to improve the time resolution of SEPMs by scanning at elevated probe translation rates can compromise the image quality due to distortions from complex convective effects, especially with larger UME probes,[12] or simply because of the reduced pixel density in the image frame.[23] Unconventional (circular and spiral)[24] scan patterns, as well as image postprocessing,[25] have been employed to overcome some limitations of slowly responding potentiometric SECM probes; however, the images did not exceed a few hundred data points, and were acquired with an acquisition rate that was 2 pixels per second at best. Although parallelized scanning routines[26,27] using linear arrays of microelectrodes probes are capable of mapping large scan areas,[28−30] such probe designs do not readily allow the acquisition of multiple frames and preclude high spatial resolution imaging.

Herein, we present the development of a high-speed scanning probe microscope for the characterization of electrochemical activity at high spatial resolution. The technique is implemented on a scanning electrochemical cell microscopy (SECCM)[31−33] platform, a scanning droplet cell technique, which is proving powerful for sensitive measurements of local electrochemical reactivity. SECCM offers reasonably fast mass-transport of redox species, low capacitance and noise levels, along with a relatively quick response time. We show that it is possible to translate this droplet probe (200 nm radius) across the substrate at rates approaching 150 μm s^{-1}. This strategy allows us to record image sequences (routinely over 100 snapshots at different potentials) with a frame rate of 0.24 fps (an image frame every 4 s), orders of magnitude higher than ever before, and a very high image pixel density of about 1000 pixels μm^{-2} (with a recording rate of up to 8000 pixels per second, again much better than existing SEPMs). This is achieved by using a nonconventional spiral scan pattern for probe positioning.

We demonstrate the high versatility of this technique on a variety of examples, from model gold dots in micropatterned self-assembled monolayers (SAMs) to the visualization of the activity of an individual single-wall carbon nanotube (SWNT) electrode at variable potentials. The characterization of nanoscopic electrocatalytic materials is exemplified by the mapping of an iridium oxide nanoparticle-decorated highly ordered pyrolytic graphite (HOPG) electrode for water splitting. These studies provide a platform for further SECCM studies and for the expansion of the concept to other SEPMs.

RESULTS AND DISCUSSION

Fast Scan Technique Considerations. SECCM utilizes a positionable double-barrel nanopipette (Figure 1a) filled with electrolyte solution, together with a quasi-reference counter electrode (QRCE) in each channel. While the nanopipette is suspended in air, a small value of ionic current flows between the nanopipette barrels through the tiny liquid droplet at the probe tip, with a bias V_2 applied between the QRCEs. Upon approaching the substrate, the liquid droplet at the tip makes meniscus contact with the specimen surface, and the value of ionic current informs on the meniscus geometry.[32] With a small vertical harmonic oscillation of the tip, it is possible to position the probe at a certain tip-to-substrate distance, *d*, relying on the value of the alternating current (AC) component of the ionic current, measured at the oscillation frequency with a lock-in amplifier (see Supporting Information section SI-1). The area of the working electrode is limited by the footprint of the liquid droplet at the specimen surface allowing amperometric measurements with a static probe, in a hopping mode or with a pipette translated laterally, while keeping *d* constant by using an AC set point value for the feedback.[33]

Implementation of the fast scanning technique imposes a set of requirements for the response time of positionable feedback and the piezoelectric positioners. The time constant of AC modulation, defined by the frequency of vertical oscillation, is limited at the upper end by the piezoelectric actuator resonance and the corresponding phase shift (with respect to the driving signal), as well as the phase lag (delay) of the positioning sensor. In the work herein, the probe oscillation was set to a few hundreds of Hz, significantly less than the resonant frequency. Considering the need to average a few harmonic oscillations to obtain a stable feedback signal, the update of the vertical position occurs at a scale of about ten milliseconds, which imposes some upper limit on the lateral rates that can be employed while achieving accurate vertical positioning. For some electrochemical techniques, bias modulation of the applied potential (instead of oscillation of the *z* position of the probe) can be implemented at up to 30 kHz, therefore enabling much faster feedback response for probe movement.[34]

Scanning the probe over the sample in the lateral direction at high speed requires piezoelectric positioning systems with high dynamic capabilities, with the positional sensor having minimal time delays. The time constant for a typical full-range translation of the $x-y$ stage is limited to approximately 1−10% of the nominal resonant frequency of the piezoelectric system,[2] making scanning at elevated scan rates particularly problematic, especially when using normal raster scan routines. Under such conditions, the actual probe position can differ from the expected pattern, contain

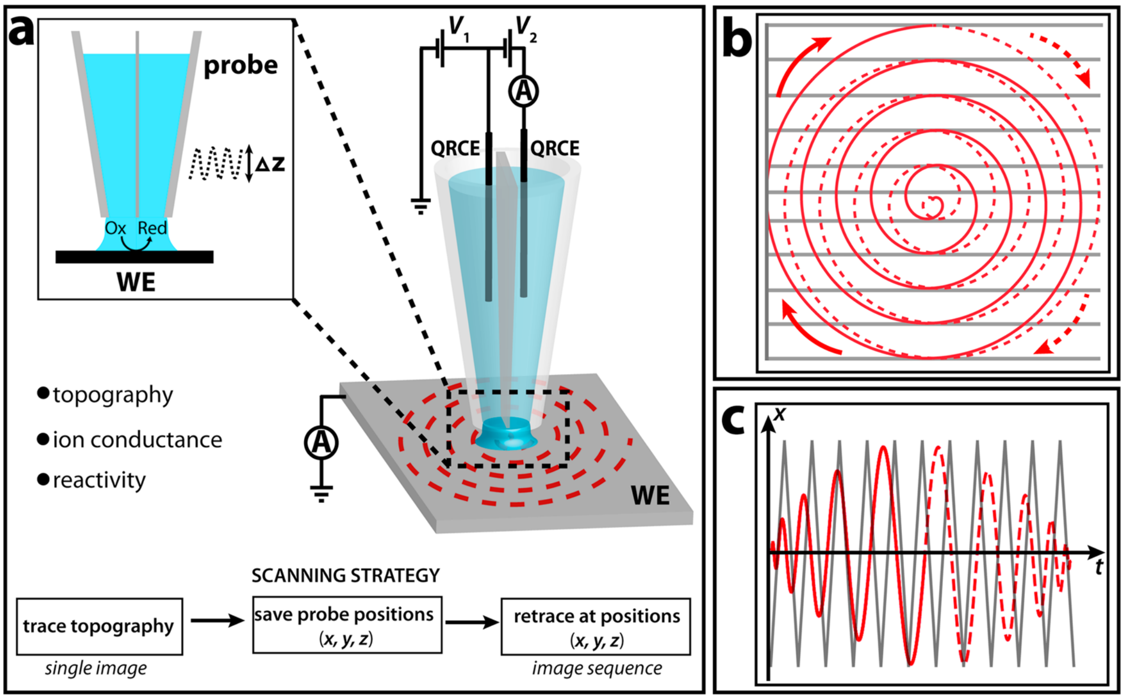

Figure 1. Schematic representation of the fast scanning SECCM routine. (a) An illustration of the SECCM operation principle. The probe is equipped with two Ag/AgCl QRCEs with a constant bias V_2 between the pipette barrels, and a variable V_1, giving rise to a substrate working electrode (WE) potential of $-(V_1 + 0.5V_2)$ *vs* Ag/AgCl QRCE. Harmonic vertical probe oscillations (indicated by Δz) induce an AC ionic current used as a positionable feedback signal in a topographical trace scan, while the recorded working electrode current, due to an electrochemical transformation, *e.g.*, $Ox + e^- \rightarrow Red$, is utilized to map the local electrochemical reactivity (see the inset in the figure). The scanning strategy involves the acquisition of substrate topography in an initial trace image at slow probe translation rate (few $\mu m\ s^{-1}$), followed by a series of quick retrace scans using the set of recorded spatial coordinates (*x*, *y*, and *z*) with a sequence of substrate potentials, applied by changing V_1. (b) The implemented spiral scan pattern for high-speed imaging (red solid and dashed lines denoting forward and reverse spirals) compared to typical raster routine (gray lines). The arrows indicate the direction of the probe translation. (c) Corresponding probe trajectory on the *x*-axis during spiral (red solid and dashed lines) and raster (gray lines) scanning.

abrupt jumps, drifts and deviations from a smooth positioning profile, resulting in higher noise level, loss of resolution or even a tip crash. In addition to attempts to improve the intrinsic mechanical performance of piezoelectric positioners,[35,36] a less complicated solution stems from the use of nonraster scan patterns, which are based on a harmonic movement simultaneously applied to both coordinate axes. In general, this concept arises from the fact that tracking smooth harmonic trajectories is usually much more reliable than triangular signals at a given frequency. Cycloid,[37] spiral[38,39] and Lissajous[40,41] patterns have been employed to improve AFM imaging dynamics.

In this work, we use sinusoidal probe tracking using an Archimedes spiral pattern (see Figure 1b) that allows continuous probe movement from the spiral center outward (forward scan) and then back inward toward the spiral origin (reverse scan), defined as a parametric curve:

$$\text{forward scan, } s_0 \le s \le \pi, \begin{cases} x = \alpha\sqrt{s}\sin(\beta\sqrt{s}) \\ y = \alpha\sqrt{s}\cos(\beta\sqrt{s}) \end{cases}$$

$$\text{reverse scan,}$$

$$\pi < s \le 2\pi - s_0, \begin{cases} x = -\alpha\sqrt{2\pi - s}\sin(\beta\sqrt{2\pi - s}) \\ y = \alpha\sqrt{2\pi - s}\cos(\beta\sqrt{2\pi - s}) \end{cases} \tag{1}$$

The scan pattern is built up based on the value of the angular coordinate, *s*, with the parameters α, β, and s_0, which determine the *xy* position of the probe on the spiral trajectory. The number of loops, *n*, on the spiral and the interloop distance, d_i, along the coordinate axis define the values of the constants

$$\alpha = \frac{nd_i}{\sqrt{\pi}} \tag{2}$$

$$\beta = 2n\sqrt{\pi} \tag{3}$$

For better control of the probe and smoother translation, 2−5 loops in the spiral center are usually removed from the pattern through the control of the offset parameter s_0.

Figure 1b,c compare the trajectory of the probe on the *x* coordinate axis for the forward and reverse scans for spiral and raster scanning routines. In raster scanning, the probe trajectory consists of a number of discrete scan lines (*e.g.*, along the *x* coordinate, called the fast scan axis), which is implemented though very different positioning profiles on the coordinate axes, whereas the probe movement on a spiral is applied as two similar harmonics (with a 90° phase shift with respect to each other). For spiral scanning, probe translation occurs with a constant lateral speed and does not involve change of the angular direction (see arrows on Figure 1b), while the angular velocity depends on the radial distance from the spiral origin. As can be seen from Figure 1c, the result is that the probe movement on the positioning axis occurs (on average) with a smaller amplitude compared to a typical triangular pattern, even though the total travel distance on the positioning axis (absolute length of the curves, shown on Figure 1c, projected on the positioning x-axis) remains constant regardless of the scan routine. This is a very important point, as the overall length of the two-dimensional trajectory of the moving probe (as shown in Figure 1b) approaches the factor 0.25π compared to the trajectory on a linear scan, and therefore allows slightly faster translation keeping the same pixel density (see details in Supporting Information SI-2). The smoother harmonic translation on the positioning axes improves the positioning accuracy (compared to the discontinuous triangular pattern) and prevents very high accelerations accompanied by the dynamic forces attributed to inertia, which occur with nanopositioners operating at high frequencies. These are particularly problematic for linear back and forth scanning. Even though the Archimedes spiral pattern does not readily allow tuning of the aspect ratio of the scan area, other harmonic scan patterns (as mentioned above) can be employed.

The fast scanning concept implemented herein circumvents the difficulties related to the time constant of positionable feedback, and the performance of the piezoelectric actuators, by using a tracing protocol at slow translation rates to record the substrate topography based on the ion conductance set point. This produces a set of coordinates (x, y, z) that are stored for a series of quick retrace scans at very high speed following a nonconventional spiral pattern (Figure 1a).

Another key consideration for high frame rate imaging is the response time of the electronics, which largely depends on the magnitude of the measured signal. In the nA current range (as typical for scanning ion conductance probes), the response time approaches a few hundred kHz. Amperometric currents in nanoscale SECM and SECCM are typically in the pA to tens of pA range for which the characteristic response frequency is several kHz (and up to multiple tens of kHz), depending on the noise level that is acceptable, so that images comprising tens of thousands pixels can be recorded within a time scale of seconds.

The final consideration is how fast amperometric probes can respond to a change in local concentration, which is governed by the local mass transport rate. For a nanoscale disc electrode (as employed, for example, for SECM), this is rapid ($\sim a^2/D = 2.5\ \mu s$, or 400 kHz for a 50 nm radius (r) probe and redox species diffusion coefficient, D, of $10^{-9}\ m^2\ s^{-1}$). The mass transport time constant in SECCM (depends on probe geometry and other parameters, easily tunable) is typically 100 times smaller (*vide infra*). These estimations provide great confidence that high resolution electrochemical images at ultrafast rates should be realizable, with the response time approaching steady-state.

Imaging Interfacial Electroactivity on Microscopic Spots on SAM-Covered Electrodes. We first demonstrate the high-speed imaging of local chemical heterogeneities in a thin film of Au covered with a patterned SAM of 1-dodecanthiol. Figure 2a demonstrates the SECCM approach for patterning SAMs, exploiting the surface modification capabilities of the technique. The local removal of SAM molecules is facilitated by localized desorption and oxidation of alkenethiolate (see Methods section for details). In this case, the size of the microdots is typically larger than the probe diameter by a factor of 1.6−2 and can be tuned by the duration of the removal protocol. The resulting pattern contains areas covered with the alkane-terminated monolayer that can block electron transfer, as well as domains of Au film (partially) free of SAM molecules. Figure 2b shows a classical ("slow", *i.e.*, performed at $2\ \mu m\ s^{-1}$ lateral translation rate) raster-scan image (consisting of 45 scan lines with 200 nm spacing with a resolution *ca.* 750 pixels μm^{-2}) of the patterned region of the sample that clearly reveals electrochemically reactive areas at the SAM-free spot-shaped locations.

The raster scan image was followed by a high-resolution zoom spiral trace (58 spiral loops with 50 nm nominal interloop distance; see the inset on Figure 2b) recorded with a probe moving at $1.6\ \mu m\ s^{-1}$ primarily for the acquisition of surface topography, but also revealing the activity and highlighting the successful implementation of the spiral scan profile (by comparison to the raster scan data). This image comprises more than 16 300 pixels with a pixel density of around 1000 pixels μm^{-2} (the original scan data comprised 10^6 pixels and have been processed by averaging). After the set of spatial coordinates was recorded and saved, a sequence of high frame rate retrace images (*ca.* 4.19 s for an image frame, probe translation rate around $98\ \mu m\ s^{-1}$) was recorded at a series of 54 substrate potential values, allowing the electroactivity of the patterned surface to be imaged as a function of electrode potential over the region where the electrochemical oxidation of ferrocene methanol (redox-active molecules in this example) took place. The applied working electrode (WE) potential started at a value of 0.25 V corresponding to the diffusion limited current and was then gradually decreased in 7.5 mV increments to shut off the reaction. Both forward and reverse spiral scans were recorded at each of the potential steps and the resulting 108 forward and reverse images (54 of each) form an image sequence.

A set of 54 snapshots resolved at different substrate potentials is conveniently represented in the form

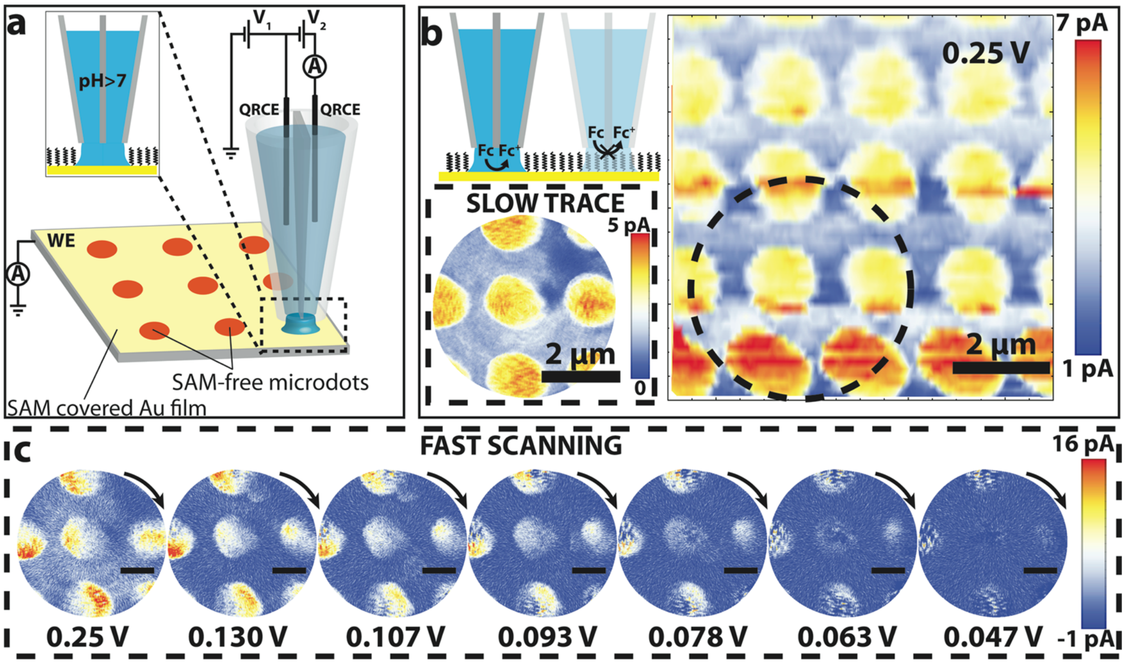

Figure 2. Imaging of interfacial electrochemical activity on patterned SAMs on Au. (a) Schematic illustration of the localized removal of alkanethiol using the SECCM setup. (b) Mapping electrochemical activity on a patterned SAM film with ferrocene methanol (Fc, 1.2 mM; KNO_3, 20 mM) redox species. Raster scan image was recorded at a slow translation rate (1.6 μm s^{-1}) at a substrate potential of 0.25 V (with 0.1 V bias applied between the QRCEs in the probe barrels, for all the images), corresponding to the diffusion-limited oxidation of Fc on Au. Dashed circular area specifies the region of the substrate, which was further imaged with high-speed spiral scans. The electrochemical image acquired during the slow topography trace scan at 0.25 V is shown as the inset, indicated with the dashed square. (c) A series of high-speed spiral retrace images (7 out of 54 combined forward and reverse scans) at various potentials. The images represent spiral scans consisting of 58 spiral loops with 50 nm interloop distance. Each image consists of ~32 500 pixels, each the average of 128 data points recorded every 2 μs with a pipette probe (tip diameter ~400 nm) translated at 100 μm s^{-1}. The arrows indicate the direction of probe translation during the spiral scan. Scale bar 1 μm. For the complete image sequence and imaging conditions please see video file nn5b02792_si_002 and section SI-4 in Supporting Information, respectively.

of a video file (see video file nn5b02792_si_002 in Supporting Information) or as a series of individual images (Figure 2c) that illustrate potential-dependent variations in the electrochemical transformations at surface heterogeneities. These high-resolution maps were constructed from both forward and reverse snapshots (recorded at the same WE potential) using the advantage of the spiral scan pattern, where the forward and reverse trajectories cover slightly different surface areas (as evident from Figure 1c), providing very high coverage of the sample surface. The data were acquired with a 25 nm step along the spiral trajectory. Thus, each presented image consists of *ca.* 32 00 data points with a resulting pixel density over 2000 pixels μm^{-2}.

Comparison between slow scan (inset on Figure 2b) and fast scan images (*e.g.*, the first frame of the image sequence on Figure 2c) indicates some difference of the current distributions on each reactive microspot with an increase of imaging rate: almost featureless, approaching uniformly active, individual dots are recorded at 1.6 μm s^{-1} (Figure 2b, inset), whereas these microdots exhibit nonuniform current profiles at high speed. The character of the inhomogeneity is similar on all the active areas of the pattern: the highest current values are registered when the scanning droplet first passes over the leading edge of the microdot and the current magnitude decays upon further probe translation over the electroactive area. This transient effect can be directly linked with the rate of diffusional mass-transport inside the SECCM pipette. Taking the very well-known expression for the transient diffusion-limited current $I(t)$ in the case of spherical mass-transport[16]

$$I(t) = nFADc_0\left[\frac{1}{\sqrt{\pi D t}} + \frac{1}{r}\right] \quad (4)$$

where n, F, D, and c_0 specify the stoichiometric number of electrons in the electrode reaction, the Faraday constant, the diffusion coefficient, and bulk redox species concentration, this relationship can be easily adapted for a nanopipette arrangement. Considering diffusion to occur in a conical fraction of a sphere of radius, r, limited by a solid angle, Ω, one can define the working electrode area, A (see details in Supporting Information SI-3). The steady-state current, I_{ss}, is

$$I_{ss} = nFADc_0\left[\frac{1}{r}\right] \quad (5)$$

and the normalized current expression, $I_{norm}(t)$, reads

$$I_{norm}(t) = \frac{I(t)}{I_{ss}} = \left[\frac{r}{\sqrt{\pi D t}} + 1\right] \quad (6)$$

This relationship suggests that the time scale required to maintain quasi-steady-state conditions is of the order of a few (or even a few tens of) milliseconds for a neutral (uncharged) redox species like ferrocene methanol using pipettes of 200 nm radius as employed herein. This is comparable to the overall transit time of the scanning nanopipette over an active microdot, resulting in a current transient behavior in the electroactive areas. The transient effect is evidenced by much less pronounced current magnitudes over the central microdot at elevated scan rates, as the probe residence time over the microdot in the center of the spiral pattern was longer. Because mass transport is well-defined, one could use this known response to correct the images for transient mass transport if so desired. As we demonstrate further in this manuscript, the temporal resolution of the SECCM technique is not always limited by the rate of diffusional mass-transport, since the choice of redox molecules allows the time constant of the transient mass flux in a probe to be improved by up to 2 orders of magnitude when employing electromigration effects (see Supporting Information SI-3). Under these conditions, the time constant of current amplification could become the most likely fundamental limitation for high fidelity steady-state current measurements, but only at much higher frame rate scanning. The response time of the current follower used for this study lies within a time scale of tens to hundreds of microseconds and is not a limitation, but one should be aware that for lower current levels, the temporal resolution could be compromised by the transient response of the current amplifiers, for which the bandwidth falls off dramatically below 1 pA V^{-1} (again, this can be modeled if needed).

Visualization of the Electroactivity of Individual Carbon Nanotubes. Recently, Güell[42,43] and Byers[44] demonstrated electrochemical imaging of individual single wall carbon nanotubes (SWNT) and their electrochemical activity toward outer and inner sphere redox couples. It is particularly interesting to follow the local electrochemical behavior of these novel carbon materials as a function of applied potential, and the advantage of high-speed scanning in this case is the possibility to track the evolution of the response at every single pixel of every image frame.

Figure 3a depicts 5 individual snapshots out of a total 100 forward and reverse images (50 of each) recorded at a frame rate of 0.1 fps. These images are constructed from spiral scans recorded at *ca.* 25 μm s^{-1} and contain around 8400 data points (each snapshot), providing an average pixel density of around 150 pixels μm^{-2}, high enough to clearly resolve the individual SWNT (~1 nm diameter) on an inert Si/SiO_2 substrate with an SECCM tip. As can be seen, the walls of the nanotube reveal fairly uniform activity toward the one-electron reduction of $[Ru(NH_3)_6]^{3+}$, throughout the potential range (−0.1 to −0.6 V *vs* Ag/AgCl QRCE) used. These results confirm previous findings[43,45] on the electroactivity of SWNTs, while also demonstrating the intrinsic advantage of the fast scanning technique to acquire a very large number of high-resolution images at different potentials, which would be a very time-consuming task using common approaches in electrochemical imaging.

One of the key requirements for high-speed SECCM implementation is the stability of the liquid meniscus at the probe tip during rapid translation. This condition is very important as deformations of the droplet geometry would result in image distortion, loss of sensitivity or resolution issues. The extracted example line profiles across a SWNT at different potentials, shown in Figure 3b, reveal the high performance capabilities of SECCM high-speed scanning (as do the images). The well-resolved edges of the nanotube and the overall measured width of the meniscus footprint, that can be deduced from the current profiles recorded across the SWNT, are consistent throughout multiple images, evidencing the stability of the liquid droplet at the probe tip even at high translation rates. The current values recorded over the SWNT exhibit rather uniform profiles, with the current increasing as the meniscus encounters the SWNT, reaching a maximum when the probe is over the SWNT and falling off as the droplet passes on. This is as seen at slow scan rates[43,45] and contrasts with the pattern shapes in Figure 2c. This difference is attributed to enhanced mass-transport, related to a combination of migration and diffusion of the redox species (with a faster bias-dependent time constant, Supporting Information, SI-3), the higher mass fluxes on isolated SWNTs,[43,45] and the longer droplet residence time due to the slower probe scan rate, allowing reasonably uniform image contrast.

The higher mass transport regime is also evidenced by the voltammetric data shown on Figure 3c, where comparison is made between a voltammogram recorded with an SECCM tip under static conditions (at a sweep rate of 100 mV s^{-1}) and averaged current values, extracted from individual frames at a set of different substrate potentials. There is a reasonably good agreement between the two sets of data, especially as the static voltammogramm is at just a small point on the SWNT, whereas the fast scan is the average of all of the currents in an image. Such a correlation indicates, first of all, the validity of the fast scanning approach and, second, shows the possibility of extracting a relatively large amount of information from a sequence of snapshots that can be presented in different ways.

It is important to point out that convective effects do not play a significant role in high-speed SECCM imaging, as the technique is intrinsically immune to convection. Convective fluxes, which may arise in the fast moving droplet, are strongly suppressed inside the pipette due to friction forces, especially with the use of

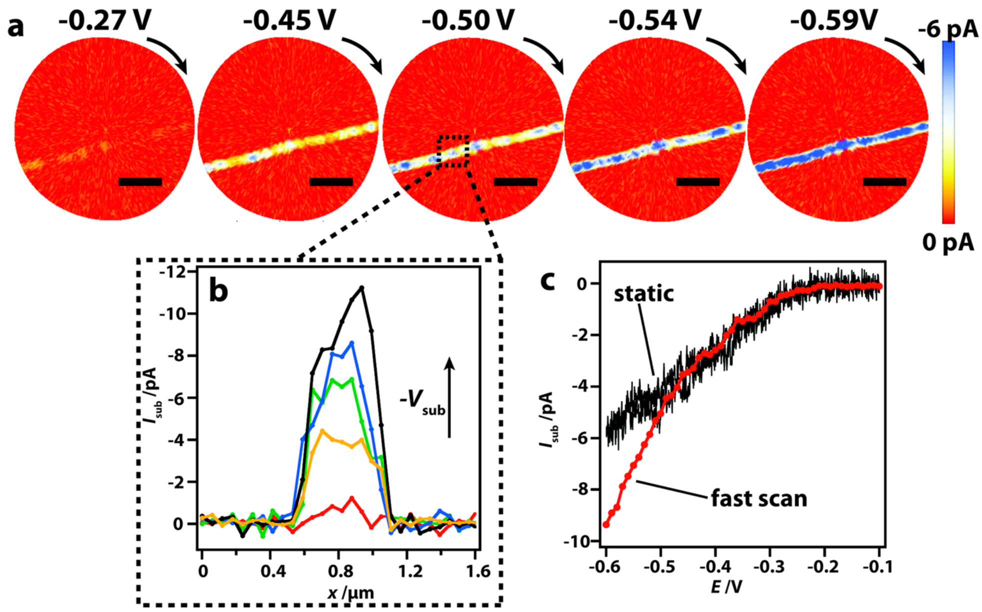

Figure 3. Visualization of the electrochemical activity of an individual SWNT. (a) Image sequence recorded over a SWNT at different potentials (5 frames out of 50 combined forward and reverse snapshots overall, see video file nn5b02792_si_003 and section SI-4 in Supporting Information) with 2 mM $Ru(NH_3)_6Cl_3$ in 50 mM phosphate buffer solution (pH 7.2) and 25 mM KCl. The displayed images are constructed from both forward and reverse scans at each potential for higher image quality. Scale bar 2 μm. (b) Line scans at a marked area of the SWNT at different substrate potentials (red, orange, green, blue, and black lines for −0.27, −0.37, −0.50, −0.54, and −0.59 V vs Ag/AgCl QRCE, respectively). The arrow indicates an increase of the (absolute) potential applied to the substrate. (c) Linear sweep voltammograms for $Ru(NH_3)_6^{3+}$ reduction at the SWNT, recorded with a static probe at one spot (black solid line) and calculated from all the currents along the central axis of the SWNT (red lines with circles) from the dynamic images.

nanopipette probes. Therefore, the measured current, which mainly depends on the mass flux within the pipette,[32] remains almost exempt from convective influence, even at very high translation rates.

Outlook: High-Speed Imaging of Electrocatalysis at Nanoscale. SECCM provides a platform to study heterogeneous catalytic reactions at the nanoscale, with the opportunity to access the activity of individual nanoparticles along with their structure using a multimicroscopy approach.[46,47] As highlighted above, the high-speed scanning method becomes even more powerful when an additional parameter, such as time or the reaction driving potential, is brought to bear on a series of images, and this is particularly the case for complex electrocatalytic surfaces.

Figure 4a provides a comparison between the activity of a bare HOPG substrate and one decorated with iridium oxide (IrO_x) nanoparticles for the water splitting oxidation reaction. At low overpotentials (below 0.5 V *vs* Ag/AgCl QRCE), the NPs do not exhibit much activity, showing a similar electrochemical response to bare HOPG, and the electrocatalytic effect becomes apparent only at relatively high (above 0.8 V) substrate potentials. The substrate data in this case are the average values across an entire image at each potential.

The set of frames in Figure 4b depicts the reactivity of NPs at a variety of substrate potentials. The striking difference to the average currents taken from the entire image is that IrO_x nanoparticles do reveal electrocatalytic characteristics at lower overpotential values (the maps show that some NPs are active already at 0.5 V *vs* Ag/AgCl QRCE), whereas the average response shows a barely detectable current enhancement (as would also be the case in a macroscopic experiment). Electrochemical imaging also allowed the evolution of NP activity to be followed as the overpotential was increased. In turn, this opens up the possibility of classifying NP clusters depending on their catalytic effect. For instance, particle aggregates "A" retain almost the same electrocatalytic activity (with respect to the average on the image) regardless of the applied potential, "B" and "C" are progressively activated with an increase of substrate potential, while cluster "D" exhibits relatively high electrocatalysis throughout almost the whole potential sweep. This difference in behavior could be due to variations in morphology of the NPs forming a particular cluster (shape, size, crystal structure, as well as arrangement of NPs in an aggregate).[47] However, further characterization of these effects was not the aim of this work. Rather, we sought to show that fast imaging of NPs on supports is possible. It is important to note that in some cases (and depending on the type and size of the NPs), detachment of NPs[48] and their removal/reposition with a moving liquid meniscus could be a possible scenario, and this would need to be assessed for a particular system. On the other hand, such effects could also offer an opportunity for the manipulation of particles on surfaces and the fabrication of nanostructures.

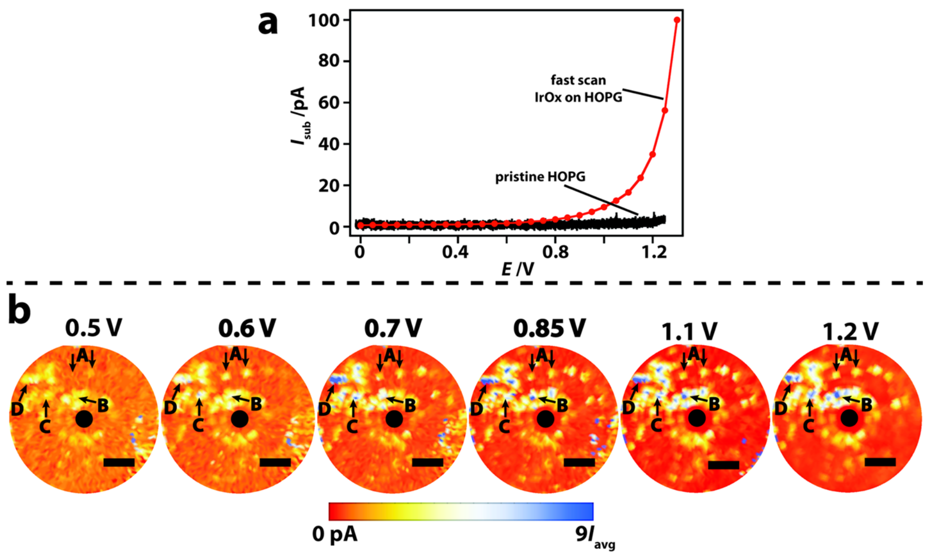

Figure 4. Electrochemical imaging of electrocatalytic water splitting at IrO_x nanoparticles electrodeposited on HOPG. (a) Linear sweep voltammogram (LSV) recorded at a fixed spot with an SECCM tip at the bare HOPG substrate (black) and a LSV calculated from the average current values over every image frame at a given substrate potential (red). (b) Image sequence recorded at a set of substrate potentials (6 forward scans out of total 30 images recorded every 12.9 s, see video file nn5b02792_si_004 and section SI-4 in Supporting Information) depicting the evolution of the rate of the electrocatalytic reaction. All measurements were in 50 mM KCl electrolyte. Nanoparticle clusters denoted as "A", "B", "C", and "D are marked. Because the current range changes dramatically in each image, the color bar is progressive with a minimum value set to 0 pA and maximum value given as a factor of the average substrate current, I_{avg}, measured by the probe (see Figure 4a for average values). Scale bar 5 μm. Black circles in the center denote areas where data were not recorded.

CONCLUSIONS

The possibility of imaging reactive heterogeneities across interfaces with high spatiotemporal resolution is very attractive for a number of reasons, notably the convenience of greatly reducing the image acquisition time, the potential to track chemical processes evolving dynamically or with a change of experimental conditions, as well as the possibility of avoiding experimental difficulties attributed to the probe and/or sample aging and fouling. In this work, an extensive roadmap introducing the capabilities of electrochemical microscopes to acquire high-resolution images at high speed has been presented.

As demonstrated, the implementation of high frame rate routines requires protocols for the rapid translation of an electrochemical nanoprobe over a specimen surface, high data recording rate and a fast probe response. We have illustrated this concept using scanning electrochemical cell microscopy (SECCM), capable of resolving surface chemical activity, with a harmonic scan profile to improve scanning performance and a strategy to trace the interface morphology followed by a series of quick retrace scans. This approach allowed the acquisition of a large number of image frames with an exceptionally high frame rate, approaching 4 s per single high-resolution snapshot (consisting of up to 1000 pixels μm^{-2}). This time scale is approximately 3−4 orders of magnitude better than that in conventional electrochemical probe imaging techniques, yet without any compromise in resolution, which−despite the much faster imaging rates—is also much better than in typical scanning electrochemical microscopy (SECM) studies.

We expect that this strategy could be extended for the use with other electrochemical imaging methods, especially SECM coupled with appropriate positional feedback techniques. A combination of SECM with the highly versatile capabilities of scanning ion conductance microscopy (SICM)[21] could further open the possibility of performing high-speed imaging even without a topographical prescan (by taking advantage of the improved time resolution of bias-modulated SICM[34] for vertical positioning at tens of kHz frequencies). The nanoscale electrodes that can be used in SECM-SICM would also ensure imaging at close to steady-state conditions.

METHODS

Scanning Electrochemical Cell Microscopy (SECCM) Setup. Nanopipettes with tip radii of approximately 200 nm were pulled from borosilicate glass double barrel (theta) capillaries (TGC150-10, Harvard Apparatus) using a laser pipette puller (P-2000, Sutter Instruments). The nanopipette probes were mounted on a mechanical micropositioner (Newport, M-461-XYZ-M) for coarse probe positioning over a sample. Precise control of the probe position (and translation) in the vertical direction was achieved with a single axis nanopositioner (Physik Instrumente, P-753.3CD). Scanning was accomplished with a high-dynamics high-precision XY nanopositioning piezoelectric stage (Physik

Instrumente, model P-733.2DD) to move the sample laterally with respect to the probe. The piezoelectric positioners were mounted inside a faraday cage, built on an optical table (Newport, RS 2000) to avoid mechanical vibrations, which incorporated acoustic insulation, vacuum insulating panels (Kevothermal) and aluminum heat sinks (aimed to reduce thermal fluctuations and drift of the piezoelectric positioners[49]). Electrochemical measurements were performed with a custom-built bipotentiostat equipped with a high sensitivity current follower to measure substrate currents with a bandwidth of 10 kHz for the current range measured herein. The SECCM setup was controlled through a FPGA card (PCIe-7852R, National Instruments) using a home-written program in a LabView interface (further details of SECCM experimental arrangement and different scanning protocols are given in section SI-1 of Supporting Information).

Chemicals. Ferrocene methanol ($FcCH_2OH$, ≥97%, Sigma-Aldrich), iridium tetrachloride hydrate (99.9%, Sigma-Aldrich), KNO_3 (≥99.0%, Sigma-Aldrich), $AgNO_3$ (Fisher Chemical), KCl (Fisher Chemical), KOH (Fisher Chemical, analytical reagent grade), $Ru(NH_3)_6Cl_3$ (98%, Sigma-Aldrich), and phosphate buffer solution (pH 7.2) (Sigma-Aldrich) were used as received. Deionized (DI) water produced by Purite Select HP with resistivity 18.2 MΩ cm (25 °C) was used to prepare aqueous solutions.

Thiol-Modified Au Film Substrates. Thiol modification of evaporated Au thin films (thickness ∼60 nm, deposited on silicon wafers) was achieved by immersing the substrates into a 5% (v/v) solution of 1-dodecanethiol (Sigma-Aldrich) in 2-propanol for at least 12 h. Electrochemical patterning of the self-assembled monolayer was performed using a strategy similar to one described by Wittstock *et al.*,[50] but adapted to be implemented with the SECCM configuration. A double barrel nanopipette filled with a slightly basic (30−50 mM KOH) aqueous solution was operated in a hopping mode (see more details in Supporting Information SI-1), so that the liquid droplet at the SECCM probe tip was brought into contact with the substrate at a set of predefined locations. Upon meniscus contact (detected as described in Supporting Information SI-1), the probe position was fixed and the substrate potential was swept to −1.4 V and then 1.2 V (*vs* Ag/AgCl QRCE in a pipette) at 0.4 V s^{-1} leading to the local removal of SAM molecules through reductive desorption and oxidative decomposition of the alkanethiolate layer.

Single Wall Carbon Nanotube (SWNT) Substrates. The SWNT sample, comprising flow-aligned SWNTs on oxidized Si wafers, was fabricated as described elsewhere.[42,44] After successful growth of SWNTs, a contact pad (Pd thin film, thickness *ca.* 50 nm) was evaporated on top of a 2 nm thick evaporated Cr adhesion layer to allow electrical connection of individual SWNTs. To facilitate the optical observation of individual nanotubes and further probe positioning over the sample, small sections of one end of the SWNTs were decorated with ensembles of Pd nanoparticles by means of electrodeposition at −0.30 V *vs* saturated calomel electrode for 200 s in 0.1 mM K_2PdCl_4 and 0.1 M $HClO_4$ solution.[51]

Decorating Highly Oriented Pyrolytic Graphite (HOPG) with Iridium Oxide (IrO_x) Nanoparticles. Electrodeposition of electrocatalyst on freshly cleaved HOPG (SPI-1 grade, SPI supplies) was performed using an electrochemical cell comprising a positionable micropipette (with typical diameter of ∼5 μm) filled with a precursor solution and containing an Ag/AgCl QRCE (the solution composition and the IrO_x nanoparticle deposition procedure were as described elsewhere[52]). The electrodeposition of nanoparticles at the HOPG working electrode (in a region limited by the footprint of the liquid meniscus on the substrate) was done by holding the substrate at a constant potential (+0.68 V *vs* Ag/AgCl QRCE for 5 s).

Conflict of Interest: The authors declare no competing financial interest.

Acknowledgment. This work was supported by the European Research Council through Project ERC-2009 AdG 247143-QUANTIF and a Marie Curie IntraEuropean Fellowship 626158 FUNICIS (D.M.). The research leading to these results has received further funding from the European Union Seventh Framework Programme (FP7/2007-2013) under grant agreement No. 329953. The authors also acknowledge Ms. Sophie L. Kinnear for her kind help with software development, Dr. Alex Colburn for high speed current amplifiers and Mr. Binoy Paulose Nadappuram for contributions to sample preparation.

Supporting Information Available: The Supporting Information is available free of charge on the ACS Publications website at DOI: 10.1021/acsnano.5b02792.

Detailed description of the SECCM setup, comparison between spiral and raster scan routines, theoretical treatment of transient SECCM responses, description of spiral scan patterns and image recording (PDF)
nn5b02792_si_002 image sequence, depicting maps of electrochemical activity as a function of the applied substrate potential on micropatterned SAM-covered electrodes (QT)
nn5b02792_si_003 image sequence, depicting maps of electrochemical activity on SWNT as a function of the applied substrate potential (QT)
nn5b02792_si_004 image sequence, depicting maps of electrochemical activity on iridium oxide nanoparticle-decorated HOPG as a function of the applied substrate potential (QT)

REFERENCES AND NOTES

1. Binnig, G.; Rohrer, H.; Gerber, C.; Weibel, E. Surface Studies by Scanning Tunneling Microscopy. *Phys. Rev. Lett.* **1982**, *49*, 57–61.
2. Fleming, A. J.; Leang, K. K. *Design, Modeling and Control of Nanopositioning Systems*; Springer: Cham, Switzerland, 2014; p 34.
3. Bryant, A.; Smith, D. P. E.; Quate, C. F. Imaging in Real Time with the Tunneling Microscope. *Appl. Phys. Lett.* **1986**, *48*, 832–834.
4. Picco, L. M.; Bozec, L.; Ulcinas, A.; Engledew, D. J.; Antognozzi, M.; Horton, M. A.; Miles, M. J. Breaking the Speed Limit with Atomic Force Microscopy. *Nanotechnology* **2007**, *18*, 044030.
5. Kodera, N.; Yamamoto, D.; Ishikawa, R.; Ando, T. Video Imaging of Walking Myosin V by High-Speed Atomic Force Microscopy. *Nature* **2010**, *468*, 72–76.
6. Tansel, T.; Taranovskyy, A.; Magnussen, O. M. *In Situ* Video-STM Studies of Adsorbate Dynamics at Electrochemical Interfaces. *ChemPhysChem* **2010**, *11*, 1438–1445.
7. Yanson, Y. I.; Schenkel, F.; Rost, M. J. Design of a High-Speed Electrochemical Scanning Tunneling Microscope. *Rev. Sci. Instrum.* **2013**, *84*, 023702.
8. Engstrom, R. C.; Weber, M.; Wunder, D. J.; Burgess, R.; Winquist, S. Measurements within the Diffusion Layer Using a Microelectrode Probe. *Anal. Chem.* **1986**, *58*, 844–848.
9. Bard, A. J. Introduction and Principles. In *Scanning Electrochemical Microscopy*, 2nd ed.; CRC Press: Boca Raton, FL, 2012; pp 1−14.
10. Bard, A. J.; Fan, F. R. F.; Pierce, D. T.; Unwin, P. R.; Wipf, D. O.; Zhou, F. Chemical Imaging of Surfaces with the Scanning Electrochemical Microscope. *Science* **1991**, *254*, 68–74.
11. Ye, H.; Lee, J.; Jang, J. S.; Bard, A. J. Rapid Screening of BiVO4-Based Photocatalysts by Scanning Electrochemical Microscopy (SECM) and Studies of Their Photoelectrochemical Properties. *J. Phys. Chem. C* **2010**, *114*, 13322–13328.
12. Fernández, J. L.; Walsh, D. A.; Bard, A. J. Thermodynamic Guidelines for the Design of Bimetallic Catalysts for Oxygen Electroreduction and Rapid Screening by Scanning Electrochemical Microscopy. M−Co (M: Pd, Ag, Au). *J. Am. Chem. Soc.* **2005**, *127*, 357–365.
13. Kueng, A.; Kranz, C.; Lugstein, A.; Bertagnolli, E.; Mizaikoff, B. Integrated AFM−SECM in Tapping Mode: Simultaneous Topographical and Electrochemical Imaging of Enzyme Activity. *Angew. Chem., Int. Ed.* **2003**, *42*, 3238–3240.
14. Sun, P.; Laforge, F. O.; Abeyweera, T. P.; Rotenberg, S. A.; Carpino, J.; Mirkin, M. V. Nanoelectrochemistry of Mammalian Cells. *Proc. Natl. Acad. Sci. U. S. A.* **2008**, *105*, 443–448.
15. Nebel, M.; Grützke, S.; Diab, N.; Schulte, A.; Schuhmann, W. Visualization of Oxygen Consumption of Single Living

Cells by Scanning Electrochemical Microscopy: The Influence of the Faradaic Tip Reaction. *Angew. Chem., Int. Ed.* **2013**, *52*, 6335–6338.
16. Bard, A. J.; Faulkner, L. R. *Electrochemical Methods—Fundamentals and Applications*, 2nd ed.; John Wiley & Sons, INC.: New York, NY, 2001; pp 171−174.
17. Etienne, M.; Dossot, M.; Grausem, J.; Herzog, G. Combined Raman Microspectrometer and Shearforce Regulated SECM for Corrosion and Self-Healing Analysis. *Anal. Chem.* **2014**, *86*, 11203–11210.
18. Ludwig, M.; Kranz, C.; Schuhmann, W.; Gaub, H. E. Topography Feedback Mechanism for the Scanning Electrochemical Microscope Based on Hydrodynamic Forces between Tip and Sample. *Rev. Sci. Instrum.* **1995**, *66*, 2857–2860.
19. McKelvey, K.; Edwards, M. A.; Unwin, P. R. Intermittent Contact−Scanning Electrochemical Microscopy (IC−SECM): A New Approach for Tip Positioning and Simultaneous Imaging of Interfacial Topography and Activity. *Anal. Chem.* **2010**, *82*, 6334–6337.
20. Takahashi, Y.; Shevchuk, A. I.; Novak, P.; Zhang, Y. J.; Ebejer, N.; Macpherson, J. V.; Unwin, P. R.; Pollard, A. J.; Roy, D.; Clifford, C. A.; et al. Multifunctional Nanoprobes for Nanoscale Chemical Imaging and Localized Chemical Delivery at Surfaces and Interfaces. *Angew. Chem., Int. Ed.* **2011**, *50*, 9638–9642.
21. Comstock, D. J.; Elam, J. W.; Pellin, M. J.; Hersam, M. C. Integrated Ultramicroelectrode-Nanopipet Probe for Concurrent Scanning Electrochemical Microscopy and Scanning Ion Conductance Microscopy. *Anal. Chem.* **2010**, *82*, 1270–1276.
22. Takahashi, Y.; Shevchuk, A. I.; Novak, P.; Murakami, Y.; Shiku, H.; Korchev, Y. E.; Matsue, T. Simultaneous Noncontact Topography and Electrochemical Imaging by SECM/SICM Featuring Ion Current Feedback Regulation. *J. Am. Chem. Soc.* **2010**, *132*, 10118–10126.
23. Etienne, M.; Layoussifi, B.; Giornelli, T.; Jacquet, D. SECM-Based Automate Equipped with a Shearforce Detection for the Characterization of Large and Complex Samples. *Electrochem. Commun.* **2012**, *15*, 70–73.
24. Kiss, A.; Nagy, G. New SECM Scanning Algorithms for Improved Potentiometric Imaging of Circularly Symmetric Targets. *Electrochim. Acta* **2014**, *119*, 169–174.
25. Kiss, A.; Nagy, G. Deconvolution of Potentiometric SECM Images Recorded with High Scan Rate. *Electrochim. Acta* **2015**, *163*, 303–309.
26. Vettiger, P.; Despont, M.; Drechsler, U.; Durig, U.; Haberle, W.; Lutwyche, M. I.; Rothuizen, H. E.; Stutz, R.; Widmer, R.; Binnig, G. K. The "Millipede" - More Than Thousand Tips for Future AFM Storage. *IBM J. Res. Dev.* **2000**, *44*, 323–340.
27. Minne, S. C.; Yaralioglu, G.; Manalis, S. R.; Adams, J. D.; Zesch, J.; Atalar, A.; Quate, C. F. Automated Parallel High-Speed Atomic Force Microscopy. *Appl. Phys. Lett.* **1998**, *72*, 2340–2342.
28. Barker, A. L.; Unwin, P. R.; Gardner, J. W.; Rieley, H. A Multi-Electrode Probe for Parallel Imaging in Scanning Electrochemical Microscopy. *Electrochem. Commun.* **2004**, *6*, 91–97.
29. Cortes-Salazar, F.; Momotenko, D.; Lesch, A.; Wittstock, G.; Girault, H. H. Soft Microelectrode Linear Array for Scanning Electrochemical Microscopy. *Anal. Chem.* **2010**, *82*, 10037–10044.
30. Lesch, A.; Vaske, B.; Meiners, F.; Momotenko, D.; Cortes-Salazar, F.; Girault, H. H.; Wittstock, G. Parallel Imaging and Template-Free Patterning of Self-Assembled Monolayers with Soft Linear Microelectrode Arrays. *Angew. Chem., Int. Ed.* **2012**, *51*, 10413–10416.
31. Ebejer, N.; Schnippering, M.; Colburn, A. W.; Edwards, M. A.; Unwin, P. R. Localized High Resolution Electrochemistry and Multifunctional Imaging: Scanning Electrochemical Cell Microscopy. *Anal. Chem.* **2010**, *82*, 9141–9145.
32. Snowden, M. E.; Güell, A. G.; Lai, S. C. S.; McKelvey, K.; Ebejer, N.; O'Connell, M. A.; Colburn, A. W.; Unwin, P. R. Scanning Electrochemical Cell Microscopy: Theory and Experiment for Quantitative High Resolution Spatially-Resolved Voltammetry and Simultaneous Ion-Conductance Measurements. *Anal. Chem.* **2012**, *84*, 2483–2491.
33. Aaronson, B. D. B.; Güell, A. G.; McKelvey, K.; Momotenko, D.; Unwin, P. R. Scanning Electrochemical Cell Microscopy: Mapping, Measuring, and Modifying Surfaces and Interfaces at the Nanoscale. In *Nanoelectrochemistry*; CRC Press: Boca Raton, FL, 2015; pp 655−694.
34. McKelvey, K.; Perry, D.; Byers, J. C.; Colburn, A. W.; Unwin, P. R. Bias Modulated Scanning Ion Conductance Microscopy. *Anal. Chem.* **2014**, *86*, 3639–3646.
35. Kindt, J. H.; Fantner, G. E.; Cutroni, J. A.; Hansma, P. K. Rigid Design of Fast Scanning Probe Microscopes Using Finite Element Analysis. *Ultramicroscopy* **2004**, *100*, 259–265.
36. Schitter, G.; Rost, M. J. Scanning Probe Microscopy at Video-Rate. *Mater. Today* **2008**, *11* (Suppl.), 40–48.
37. Yong, Y. K.; Moheimani, S. O.; Petersen, I. R. High-Speed Cycloid-Scan Atomic Force Microscopy. *Nanotechnology* **2010**, *21*, 365503.
38. Mahmood, I. A.; Moheimani, S. O. Fast Spiral-Scan Atomic Force Microscopy. *Nanotechnology* **2009**, *20*, 365503.
39. Ziegler, D.; Meyer, T. R.; Farnham, R.; Brune, C.; Bertozzi, A. L.; Ashby, P. D. Improved Accuracy and Speed in Scanning Probe Microscopy by Image Reconstruction from Non-Gridded Position Sensor Data. *Nanotechnology* **2013**, *24*, 335703.
40. Yong, Y. K.; Bazaei, A.; Moheimani, S. O. R.; Allgower, F. In *Design and Control of a Novel Non-Raster Scan Pattern for Fast Scanning Probe Microscopy*, Advanced Intelligent Mechatronics (AIM), 2012 IEEE/ASME International Conference on, 11−14 July 2012; IEEE: Hoboken, NJ, **2012**; pp 456−461.
41. Tuma, T.; Lygeros, J.; Kartik, V.; Sebastian, A.; Pantazi, A. High-Speed Multiresolution Scanning Probe Microscopy Based on Lissajous Scan Trajectories. *Nanotechnology* **2012**, *23*, 185501.
42. Güell, A. G.; Meadows, K. E.; Dudin, P. V.; Ebejer, N.; Macpherson, J. V.; Unwin, P. R. Mapping Nanoscale Electrochemistry of Individual Single-Walled Carbon Nanotubes. *Nano Lett.* **2014**, *14*, 220–224.
43. Güell, A. G.; Ebejer, N.; Snowden, M. E.; McKelvey, K.; Macpherson, J. V.; Unwin, P. R. Quantitative Nanoscale Visualization of Heterogeneous Electron Transfer Rates in 2D Carbon Nanotube Networks. *Proc. Natl. Acad. Sci. U. S. A.* **2012**, *109*, 11487–11492.
44. Byers, J. C.; Güell, A. G.; Unwin, P. R. Nanoscale Electrocatalysis: Visualizing Oxygen Reduction at Pristine, Kinked, and Oxidized Sites on Individual Carbon Nanotubes. *J. Am. Chem. Soc.* **2014**, *136*, 11252–11255.
45. Nadappuram, B. P.; McKelvey, K.; Byers, J. C.; Güell, A. G.; Colburn, A. W.; Lazenby, R. A.; Unwin, P. R. Quad-Barrel Multifunctional Electrochemical and Ion Conductance Probe for Voltammetric Analysis and Imaging. *Anal. Chem.* **2015**, *87*, 3566–3573.
46. Kleijn, S. E. F.; Lai, S. C. S.; Miller, T. S.; Yanson, A. I.; Koper, M. T. M.; Unwin, P. R. Landing and Catalytic Characterization of Individual Nanoparticles on Electrode Surfaces. *J. Am. Chem. Soc.* **2012**, *134*, 18558–18561.
47. Lai, S. C. S.; Dudin, P. V.; Macpherson, J. V.; Unwin, P. R. Visualizing Zeptomole (Electro)Catalysis at Single Nanoparticles within an Ensemble. *J. Am. Chem. Soc.* **2011**, *133*, 10744–10747.
48. Lai, S. C. S.; Lazenby, R. A.; Kirkman, P. M.; Unwin, P. R. Nucleation, Aggregative Growth and Detachment of Metal Nanoparticles During Electrodeposition at Electrode Surfaces. *Chem. Sci.* **2015**, *6*, 1126–1138.
49. Kim, J.; Shen, M.; Nioradze, N.; Amemiya, S. Stabilizing Nanometer Scale Tip-to-Substrate Gaps in Scanning Electrochemical Microscopy Using an Isothermal Chamber for Thermal Drift Suppression. *Anal. Chem.* **2012**, *84*, 3489–3492.
50. Wittstock, G.; Hesse, R.; Schuhmann, W. Patterned Self-Assembled Alkanethiolate Monolayers on Gold. Patterning and Imaging by Means of Scanning Electrochemical Microscopy. *Electroanalysis* **1997**, *9*, 746–750.

51. Dudin, P. V.; Snowden, M. E.; Macpherson, J. V.; Unwin, P. R. Electrochemistry at Nanoscale Electrodes: Individual Single-Walled Carbon Nanotubes (SWNTs) and SWNT-Templated Metal Nanowires. *ACS Nano* **2011**, *5*, 10017–10025.
52. Nadappuram, B. P.; McKelvey, K.; Al Botros, R.; Colburn, A. W.; Unwin, P. R. Fabrication and Characterization of Dual Function Nanoscale pH-Scanning Ion Conductance Microscopy (SICM) Probes for High Resolution pH Mapping. *Anal. Chem.* **2013**, *85*, 8070–8074.